Crystal structure of Ni-sorbed synthetic vernadite: A powder X-ray diffraction study

Sylvain Grangeon, Bruno Lanson, Martine Lanson, Alain Manceau

Crystal structure of Ni-sorbed synthetic vernadite: A powder X-ray diffraction study

Sylvain Grangeon*, Bruno Lanson, Martine Lanson, and Alain Manceau

[1]Mineralogy & Environments Group, LGCA, Maison des Géosciences, BP53, Université Joseph Fourier – CNRS, 38041 Grenoble Cedex 9, France

* E-mail: Sylvain.Grangeon@obs.ujf-grenoble.fr

Keywords: δ-MnO_2, vernadite, birnessite, Mn oxide, turbostratic structure, XRD, X-ray diffraction, crystal chemistry, Ni sorption

Running title: Structure of Ni-sorbed vernadite

ABSTRACT

Vernadite is a nanocrystalline turbostratic phyllomanganate ubiquitous in the environment, which contains nickel in specific settings such as oceanic sediments. To improve our understanding of nickel uptake in this mineral, two series of synthetic analogs to vernadite (δ-MnO_2) were prepared with Ni/Mn atomic ratios ranging from 0.002 to 0.105 at pH 4 and from 0.002 to 0.177 at pH 7, and their structures characterised using X-ray diffraction (XRD). The δ-MnO_2 nano-crystals are essentially monolayers with coherent scattering domain sizes of ~10 Å perpendicular to the layer and of ~55 Å in the layer plane. The layers contain an effective proportion of ~18% vacant octahedral sites, regardless of the Ni content. At Ni/Mn ratios <1%, XRD has no sensitivity to Ni, and the layer charge deficit is apparently entirely balanced by interlayer Mn, Na, and protons. At higher Ni/Mn ratios, Ni occupies the same site as interlayer Mn above and/or below layer vacancies together with sites along the borders of the MnO_2 layers, but the layer charge is balanced differently at the two pH values. At pH 4, Ni uptake is accompanied by a decrease in structural Na and protons, whereas interlayer Mn remains strongly bound to the layers. At pH 7, interlayer Mn is less strongly bound and partly replaced by Ni. The results also suggest that the number of vacant layer sites and multivalent charge-compensating interlayer species are underestimated in the current structure models for δ-MnO_2.

Introduction

The phyllomanganate vernadite, like its synthetic analog δ-MnO_2 (McMurdie, 1944), is a nanosized and turbostratic variety of birnessite, that is a layered manganese oxide consisting of randomly stacked layers composed of MnO_6 octahedra (Bricker, 1965; Giovanoli, 1980). In the structure model presently available for δ-MnO_2 (Villalobos *et al.*, 2006), the nano-sized layers contain only Mn^{4+} cations and vacant octahedral sites (6%), whose charge is compensated for by interlayer Na^+ ($Na_{0.24}(H_2O)_{0.72}[Mn^{4+}_{0.94},vac_{0.06}]O_2$). Vernadite likely forms, at least in part, from the biologically-mediated oxidation of Mn(II) (Tebo *et al.*, 2004). For example, different strains of fungi and bacteria have been shown to produce vernadite-like oxides (Mandernack *et al*., 1995; Jurgensen *et al.*, 2004; Tebo *et al.*, 2004, 2005; Webb *et al.*, 2005; Miyata *et al.*, 2006; Villalobos *et al.*, 2006). Their high metal sorption capacities result from the combination of small particle size, which induces a high number of border sites, and of vacant layer sites, which create a locally strong charge deficit.

As a result of this reactivity, vernadite has a key influence on the mobility of metals in a variety of environments. For example, Ni and other trace metals were reported to be associated with vernadite-like minerals in oceanic and lake ferromanganese nodules and crusts (Aplin and Cronan, 1985; Bogdanov *et al.*, 1995; Koschinsky and Halbach, 1995; Lei and Boström, 1995; Exon *et al.*, 2002; Koschinsky and Hein, 2003; Bodei *et al.*, 2007; Peacock and Sherman, 2007a; Manceau *et al.*, 2007a). Similarly, in manganese coatings deposited on water-processing filtration sands nickel is essentially bound to vernadite (Manceau *et al.*, 2007b). Understanding the reactivity of vernadite with nickel and the stability of Ni-complexes requires gaining insights into the metal-mineral interactions occurring at the atomic scale. The ability of usual diffraction methods, such as the Rietveld

method, is however impaired by the minute size and extreme stacking disorder of these compounds.

This article reports structure models for Ni-sorbed δ-MnO_2 using X-ray diffraction (XRD), and chemical data. The layer and interlayer crystal structure and the mean number of stacked layers were determined from the trial-and-error simulation of the *hk* scattering bands and of the 00*l* reflections (Drits and Tchoubar, 1990; Plançon, 2002). This modelling approach was applied previously on synthetic and natural phyllomanganates differing in chemical composition and density of structural defects (Chukhrov *et al.*, 1985; Lanson *et al.*, 2000, 2002a, 2002b, 2008; Gaillot *et al.*, 2003, 2005, 2007; Villalobos *et al.*, 2006). The validity of the structure models was assessed from the comparison with Ni K-edge extended X-ray absorption fine structure (EXAFS) data and from bond valence calculations. Finally, structural mechanisms for the sorption of Ni onto δ-MnO_2 crystals are proposed from the integration of all results.

Experimental methods

Synthesis of δ-MnO_2 and Ni sorption protocol

The sample preparation was described previously (Manceau *et al.*, 2007b). Briefly, suspensions of Na-rich δ-MnO_2 were prepared following the protocol of Villalobos *et al.* (2003), kept hydrated for several days, and then equilibrated at pH 4 or pH 7 and enriched afterwards in Ni at constant pH by the slow (0.4 mL/min) dropwise addition of a $5x10^{-4}$ mol/L $Ni(NO_3)_2$ solution. After 12 h of equilibration, the suspensions were filtered, rinsed with a few mL of deionized water, and freeze-dried. The samples are named as in the previous study (Table 1).

Chemical analysis

The mean oxidation degree of manganese was determined by potentiometric titration using Mohr salt [$(NH_4)_2Fe(SO_4)$] and $Na_4P_2O_7$ (Lingane and Karplus, 1946; Vetter and Jaeger, 1966). Three measurements were made on each sample, and a reference was measured after each sample to ensure the absence of bias due to titrant ageing. Total Mn, Ni and Na contents were determined with a Perkin-Elmer Optima 3000 ICP-AES (Inductively Coupled Plasma – Atomic Emission spectrometer) on aliquots of solutions prepared from ~5 mg powder digested in ~15 mL NH_3OHCl (0.7 mol/L, pH 1.9) for 1 minute. Results are reported in Table 1.

X-ray diffraction

Powder X-ray diffraction (XRD) patterns were recorded over the 5-80 °2θ angular range (17.6 Å – 1.20 Å) with a 0.04 °2θ angular step and 40 seconds counting time per step, using a D5000 diffractometer equipped with a SolX solid-state detector from Baltic Scientific Instruments and CuKα radiation. Simulations were performed successively on the high- (30-80 °2θ CuKα) and low-angle (5-30 °2θ CuKα) regions of the diffractograms. The high-angle region is dominated by the scattering from two-dimensional *hk* bands, *hkl* reflections being unresolved owing to the random layer stacking (random rotations and/or translations in the *a*-*b* plane are systematic between adjacent layers). The in-plane unit-cell parameters (*a* and *b*) were determined from the position of the band at ~1.41 Å (31,02 band using a C-centered unit-cell, in which *a* and *b* axes are orthogonal), which is little affected by other structural parameters. The unit-cell parameters relative to the layer stacking (*c* parameter, and α and β angles) and the space group were not determined because of the turbostratic stacking which leads to the lack of any 3D periodicity. Despite the intrinsic structural disorder, atomic coordinates and site occupancies for layer (Mn) and interlayer (Na, Ni, Mn) cations were

however obtained from the simulation of the 11,20 band (at ~2.42 Å), because its profile is strongly modulated by the crystal structure factor (Villalobos *et al.*, 2006; Drits *et al.*, 2007; Lanson *et al.*, 2008). The size of the coherent scattering domains (CSDs), which are supposed to have a disk-like shape in the *a*-*b* plane, also was derived from the modelling of the 11,20 band profile. The low-angle region, which contains 00*l* reflections, was used to verify the lamellar character of the samples and to calculate the size of the CSDs along the c^* direction (i.e. the mean number of layers stacked coherently) and the *d*(001) basal distance. Atomic positions and occupancies were constrained to be identical for the simulation of the two sets of reflections.

The background was supposed to decrease linearly over the two angular ranges. The quality of fit was evaluated with the R_{wp} and GoF (Goodness of fit = R_{wp}^2/R_{exp}^2) parameters (Attfield *et al.*, 1988; Howard and Preston, 1989). The uncertainty on the different structure parameters could not be determined quantitatively because the trial-and-error approach, required by the turbostratic nature of the samples investigated, does not allow the calculation of a covariance matrix. However, the uncertainty on interlayer cation site occupancy can be estimated to ±1% from the comparison of experimental and calculated XRD patterns (Manceau *et al.*, 1997). Further qualitative assessment of uncertainties is provided by Villalobos *et al.* (2006) and Lanson *et al.* (2008) using sensitivity tests.

Results

Qualitative description of XRD profiles

The diffractograms of Ni-sorbed δ-MnO_2 are typical of turbostratic birnessite-like crystals (Fig. 1 – Drits *et al.*, 1997; Villalobos *et al.*, 2006). The peaks at ~7.6 Å and ~3.7 Å correspond to basal reflections 001 and 002, although they do not form a strictly rational series (Lanson *et al.*, 2008). The broad and asymmetric scattering maxima at ~2.42 Å,

~1.41 Å and ~1.22 Å are indexed as 11,20, 31,02 and 22,40 bands, respectively, using a C-centred unit cell (Drits *et al.*, 1997, 2007; Webb *et a*l., 2005; Villalobos *et al.*, 2006; Lanson *et al.*, 2008). For all samples, the *d*-spacings of the 11,20 and 31,02 bands are in a ratio (~1.72) close to √3, indicative of a hexagonal layer symmetry. The symmetry of the 31,02 band profile also supports a layer unit cell that is hexagonal. If the layer unit cell were orthogonal this band would split into separate 31 and 02 bands and appear asymmetric (Drits *et al.*, 2007; Lanson *et al.*, 2008).

At first glance, all XRD patterns look similar, with the systematic presence of poorly defined 00*l* reflections in the low-angle region, and of *hk* bands exhibiting similar relative intensities in the high-angle one. Upon closer examination, it appears however that only NidBi2-4 and NidBi11-4, and NidBi2-7 and NidBi11-7, are statistically indistinguishable (Fig. 1). Therefore, in the following NidBi11-4 and NidBi11-7 are omitted. The 00*l* reflections are more intense at pH 7 than pH 4, and decrease with increasing Ni content for the pH 4 series. The broad hump at 50-55 °2θ becomes more pronounced as the Ni content increases in the two pH series (Fig. 1).

As shown by Drits *et al.* (2007), the modulations of the 11,20 band can be interpreted in structural terms. Specifically, XRD data resemble computations performed assuming hexagonal layer symmetry and ~17% vacant layer sites capped by interlayer $Mn^{2+/3+}$ in triple-corner sharing position (TC linkage, Fig. 2 – Manceau *et al.*, 2002). The above described "hump" is indeed characteristic of a high number (>10%) of layer vacancies capped by "heavy" cations (Figs. 13a, b in Drits *et al.*, 2007). Furthermore, "heavy" interlayer cations are located mainly in TC rather than TE (triple edge sharing – Fig. 2) position (see Fig. 13c in Drits *et al.*, 2007). We can thus hypothesize as a starting model, that all Ni-sorbed δ-MnO_2 samples are turbostratic phyllomanganates, whose layers have a hexagonal symmetry and

158 bear significant amount of vacancies (>10%) capped mainly by “heavy” interlayer species
159 (Mn or Ni) in TC or DC sites.

160 Combining this tentative structure model and the chemical data reported in Table 1, the
161 following generic structural formula can be proposed:

162 $$H^{+}_{a}Ni^{2+}_{b}Mn^{2+/3+}_{c}Na^{+}_{d}(H_2O)_e[Mn^{4+}_{f}Mn^{3+}_{g}Ni^{2+}_{h}vac_i]O_2$$

163 where species between square brackets are located within the octahedral layer (vac stands for
164 vacant layer sites) and those to the left of the brackets are interlayer species. The number of
165 adjustable variables can be substantially reduced by physical and chemical constrains. First,
166 EXAFS showed that Ni is predominantly located at TC and DC sites at pH 4 and pH 7 and
167 Ni/Mn > 1% (Manceau *et al.*, 2007b – <*d*(Ni-O)> ~2.05±0.02 Å). At lower Ni concentration,
168 Ni partly fills vacant layer sites (E sites) in proportions which depend on the pH. This fraction
169 was ignored in XRD simulations ($h = 0$) because it is minor (< 1%) compared to the number
170 of Mn atoms in the manganese layers, and because Mn and Ni have similar scattering factors.
171 Interlayer Mn cations are octahedrally coordinated as consistently reported in similar
172 structures (Chukhrov *et al.*, 1985; Silvester *et al.*, 1997; Villalobos *et al.*, 2006; Lanson *et al.*,
173 2008). In the simulations, sodium was coordinated to three water molecules as reported
174 previously (Post and Veblen, 1990; Villalobos *et al.*, 2006). Finally, relative amounts of Mn^{4+},
175 Mn^{3+}, Ni^{2+}, and Na^{+} were constrained to their chemical values (Table 1), and protons were
176 eventually introduced to ensure the electro-neutrality of the structure. Parameters adjusted
177 during the fitting process were thus limited to the distribution of Mn^{3+} cations between layer
178 and interlayer sites, the position of interlayer Na^{+} and coordinated H_2O molecules, and the
179 coordinates of interlayer Mn, Ni, and associated H_2O molecules along the *c** axis.

180

181

Simulation of the high-angle (30-80 °2θ Cu-Kα) region

In a first attempt, atomic coordinates were assumed to be identical for all samples, as the synthesis and sorption procedures were analogous, and only site occupancies were adjusted, together with unit-cell parameters and CSD sizes. Once the main features of all XRD patterns were satisfactorily reproduced, atomic coordinates were adjusted for each sample, but the fit to the data could not be improved significantly. Atomic positions are thus identical for all samples which differ only by their respective unit-cell parameters, CSD sizes, and their contents of the various interlayer species (Tables 2, 3). The best fits to the XRD data are shown in Figure 3. The plausibility of the proposed models was assessed by calculating the valence of all atoms in the structure (Table 4 – Brown, 1996), which is an efficient way to constrain the model (Gaillot *et al.*, 2003).

The crystals are systematically nanosized (50-56 Å in diameter in the layer plane). Layers contain a significant amount (16-18.5%) of vacant sites, which are capped on one or the two sides by octahedrally coordinated Mn^{3+} and/or Ni^{2+}, depending on the Ni/Mn loading and on the equilibration pH. Na^{+} and H^{+} compensate for the remainder of the negative layer charge. With increasing Ni loading, the number of Ni complexes increases at the expense of Na^{+} and/or interlayer Mn, depending on the pH series. At pH 4, Ni preferentially replaces Na^{+}, the number of ^{TC}Mn remaining constant within error, whereas Ni replaces both Na^{+}, ^{TC}Mn, and ^{TE}Mn at pH 7.

Interlayer Mn^{3+} and Ni^{2+} are octahedrally coordinated and located either above/below vacant layer sites or in TE sites. Sodium is located in the interlayer mid-plane coordinated to three water molecules at 2.30 Å, 2.89 Å and 2.95 Å (Fig. 4). The first distance is shorter than commonly observed (i.e. ~2.45 Å – Angeli *et al.*, 2000) but has already been reported in the literature (Brown, 1977). The prevalence of monolayers precludes oxygen atoms from adjacent layers to provide bond valence to Na, and thus favours strong interactions with

207 interlayer H_2O molecules. The first coordination sphere of Na^+ is limited to ~3.0 Å, consistent
208 with theoretical studies (Delville, 1992). However, the sum of bond valence with H_2O
209 molecules (O6) and layer oxygen (O1) is not sufficient to fully compensate the Na^+ charge
210 (Table 4), as discussed in the following section. The position of H_2O molecules coordinated to
211 interlayer Na^+ allows for the formation of strong H-bonds with layer oxygen atoms (O_{layer}),
212 with $d(H_2O\text{-}O_{layer})$ = 2.71 Å.

213 To match the measured mean oxidation degree of Mn, Mn^{3+} cations have to be included
214 in the octahedral layers, but the number of $^{E}Mn^{3+}$ remains limited, peaking at ~9% of layer
215 octahedra for sample NidBi2-4 (Table 1). This low number is consistent with the hexagonal
216 symmetry of the layer (Gaillot *et al.*, 2005, 2007; Manceau *et al.*, 2005). The in-plane *b* unit-
217 cell parameter (2.835 Å ≤ *b* ≤ 2.840 Å) are similar to those reported previously for δ-MnO_2
218 (2.838 Å – Villalobos *et al.*, 2006). The sensitivity to this parameter was assessed with sample
219 NidBi105-4 from the variation of R_{wp} as a function of the *b* parameter ($a = \sqrt{3} \times b$ – Fig. 5).
220 The estimated error on *b* is ±0.001 Å.

221

222 *Simulation of the low-angle (5-30 °2θ) region*

223 The position, amplitude, and width of the two 00*l* reflections present over this low-angle
224 region were simulated using the optimal structure models and adjusting only the out-of-plane
225 *d*(001) parameter and CSD size along the c^* direction. Experimental data were fitted with
226 mean CSD sizes of 9.5/7.3 = 1.3 to 15.3/7.3 = 2.1 layers (Table 2, Fig. 6). Thus, most crystals
227 consist of isolated layers. When a diffracting crystallite contains two or more layers, its layer
228 stacking is random (i.e., turbostratic) as no significant modulations are visible on *hk* bands
229 (see Lanson *et al.*, 2008, for a discussion). The *d*(001) basal distance determined (7.3 Å) is
230 slightly higher than usually reported for both ordered and disordered birnessites (7.2 Å). This

231 increased basal distance is consistent with the weak bonding between adjacent layers
232 supported by the small CSD sizes.
233
234 **Discussion**
235 *Composition of the interlayer*
236 Except for Na, all atomic positions are consistent with those previously determined for metal-
237 sorbed birnessite-like compounds, either well or poorly crystallised (Manceau *et al.*, 1997,
238 2002; Lanson *et al.*, 2002b, 2008; Villalobos *et al.*, 2006). The Na^+ position [(-0.525, 0, 1/2)
239 and equivalent positions] however provides this cation with an environment similar to that
240 commonly reported in Na-bearing disordered birnessite (Villalobos *et al.*, 2006; Lanson *et al.*,
241 2008) with $d(Na\text{-}O_{layer}) \sim 2.66$ Å. Na^+ coordination consists essentially of adjacent O_{layer}
242 atoms and interlayer H_2O molecules, however failing to fully compensate the charge of this
243 cation (Table 4). The nanocrystalline character of δ-MnO_2, and specifically the prevalence of
244 monolayers, may account for the compensation of the remaining charge, as H_2O molecules
245 hydrating the crystals may actually contribute to charge compensation. For crystals composed
246 of more than one layer, O_{layer} from adjacent layers could also contribute to compensate the
247 charge of interlayer Na, but sample turbostratism precludes the calculation of this bond
248 valence.
249 The sensitivity of XRD patterns calculated for turbostratic birnessite to small variations
250 of the site coordinates or occupancies has been discussed previously (Villalobos *et al.*, 2006;
251 Drits *et al.*, 2007; Lanson *et al.*, 2008), and is not discussed further here to assess model
252 robustness. The proposed structure model implies the replacement of interlayer Mn and Na
253 cations by interlayer Ni (Table 3) with increasing Ni/Mn content. If based on XRD data only,
254 this model could appear questionable as XRD is sensitive only to the distribution of electronic
255 density but does not provide element-specific information. One could thus argue that XRD

256 simulation demonstrates essentially an increase of the electronic density above/below vacant
257 layer sites with increasing Ni/Mn content, especially for the pH 7 series. This modification of
258 the electron density distribution could possibly result from a limited adsorption of Ni
259 assuming a constant number of interlayer Mn. Various constrains allow rejection of this
260 alternative structure model. First, the two elements do not have the same *z*-coordinates, thus
261 allowing their differentiation in the interlayer. Second, the mean oxidation degree of Mn
262 increases with increasing Ni loading, showing that the number of Mn^{3+}, which is dominantly
263 present as an interlayer species, decreases with increasing Ni/Mn content. In addition, a Ni^{2+}-
264 for-Na^{+} exchange would lead to a strong excess of charge in δ-MnO_2 structure, whereas the
265 Ni^{2+}-for-Mn^{3+} exchange avoids this effect despite the increased number of interlayer cations
266 above/below vacant layer sites. Finally, the evolution of the Ni/Mn ratio requires increasing
267 the Ni content in the XRD simulations. EXAFS showed that Ni was not present as a
268 precipitate (Manceau *et al.*, 2007b), that would most likely have been detected also by XRD.
269 The hypothesis of Ni sorption on the edges of δ-MnO_2 crystals at a octahedral layer site (E
270 site – Fig. 2) may also be rejected as it would lead to a significant increase of the CSD size of
271 these crystals within the *a*-*b* plane. The sorption of 2 Ni octahedra on the edges of δ-MnO_2
272 crystals would increase indeed the CSD size by 20-25% (from 54 to 66 Å in diameter), which
273 would be easily detected by XRD owing to the high sensitivity of calculated patterns to this
274 parameter (Villalobos *et al.*, 2006). For sample NidBi105-4, such an increase of the CSD size
275 would lead to R_{wp} and GoF values of 7.04% and 6.62, respectively, about two times the value
276 of the optimal model (5.00%, and 3.33, respectively – Fig. 3). Such sorption would impact
277 also the EXAFS signal, inconsistent with the data since edge-sharing Ni-Mn pairs are
278 excluded at high Ni/Mn (Manceau *et al.*, 2007b).

279 The local environment of Ni can be constrained further from Ni-EXAFS results
280 obtained on the same samples by Manceau *et al.* (2007b). According to these results, Ni sorbs

281 predominantly as ^{TC}Ni and ^{DC}Ni complex at pH 4-7 and Ni/Mn ratios > 1%. The XRD and
282 EXAFS models are therefore consistent as the ^{TC}Ni and ^{DC}Ni sites are equivalent for XRD,
283 the investigated solids being too disordered to allow the discrimination of small differences in
284 atomic coordinates. Despite the partial sorption of Ni at DC sites, that is on particle edges
285 (Manceau *et al.*, 2007b), no increase of the CSD is observed. This observation is possibly due
286 to the multiplicity of Ni sorption sites (E, TC, DC) and to the possibility for Ni atoms to sorb
287 on the two DC sites apart the same edge octahedron. Our results also agree with those
288 reported by Peacock and Sherman (2007b) in their study of Ni sorption on synthetic
289 hexagonal birnessite, a well crystallised phyllomanganate in which one sixth of the layer sites
290 are vacant and capped by interlayer Mn^{3+} (Drits *et al.*, 1997; Silvester *et al.*, 1997; Lanson *et*
291 *al.*, 2000). At pH 7, Peacock and Sherman (2007b) observed that ~90% of total Ni occupy TC
292 sites. The apparent absence of ^{DC}Ni in their study is likely related to the larger lateral
293 dimension of birnessite layers relative to δ-MnO_2 as the proportion of border sites, and thus
294 surface reactivity of phyllomanganates in general, tremendously decreases when layer size
295 increases (Tournassat *et al.*, 2002; Villalobos *et al.*, 2005; Webb *et al.*, 2005).

296 Sorption of metal cations in TE site has been seldom described (Lanson *et al.*, 2002b,
297 2008). Here, it may be favoured by the combined effects of the high density of interlayer
298 cations in TC position and the probable presence of some layer Mn^{3+} cations (Table 1). The
299 occupancy of the two TC positions apart the same vacancy induces electrostatic repulsion,
300 especially when Ni^{2+} is facing a Mn^{3+} cation, that can be minimised by moving one cation in
301 TE position. In addition, the combined presence of Mn^{3+} cations and of vacant sites in the
302 octahedral layers results in the strong undersaturation of some O_{layer} atoms that is best
303 compensated for by the presence of interlayer cations in both TC and TE sites (Lanson *et al.*,
304 2002b).

305

306 *Ni sorption mechanism*

307 Although similar structure models were obtained for the two δ-MnO_2 series, the mechanism
308 of Ni sorption likely differs at the two pHs, as attested macroscopically by the twofold
309 increase in the evolution of the Mn mean oxidation degree with Ni loading at pH 7 (Fig. 7).
310 Chemical data and XRD simulations suggest that at pH 4 Ni^{2+} replaces preferentially Na^{+} and
311 H^{+}, Mn^{3+} being strongly bound to the octahedral layers, whereas Ni^{2+} more readily exchanges
312 for Mn^{3+} at pH 7. This contrasting behaviour could result from the higher number of Mn^{3+}
313 cations in the octahedral layers at low pH. As discussed above, the coexistence in octahedral
314 layers of vacant layer sites and Mn^{3+} cations induces a strong undersaturation of O_{layer} atoms,
315 and therefore favours the binding of high-charge interlayer cations such as Mn^{3+}.

316

317 *Comparison to structure models previously reported for δ-MnO_2*

318 For a long time, the structure of δ-MnO_2 has been controversial. This compound, now known
319 to be analogous to vernadite and turbostratic birnessite, was first reported by McMurdie
320 (1944), and described as poorly crystalline cryptomelane (McMurdie and Golovato, 1948). In
321 contrast, Feitknecht and Marti (1945) suggested a lamellar structure similar to pyrochroïte.
322 The structural analogy between δ-MnO_2 and birnessite was suggested by Giovanoli (1969,
323 1980), and a structure model was proposed recently by Villalobos *et al.* (2006) using XRD
324 and EXAFS spectroscopy. Despite the availability of structure models, and the demonstrated
325 potential for structure characterization (Drits *et al.*, 2007), δ-MnO_2 is however commonly
326 referred to as "amorphous manganese oxide" or as "hydrous manganese oxide – HMO" (Xu
327 and Yang, 2003; Boonfueng *et al*., 2005; Huang *et al*., 2007) without precision on important
328 structural parameters such as the origin of the layer charge (vacant layer sites vs Mn^{3+} in the
329 layers).

The structure model proposed here differs in three points from the model proposed by Villalobos *et al.* (2006), for another sample synthesized following the same protocol. Previously, the structure was considered to contain only Mn^{4+}, because the average oxidation degree obtained by the oxalate and iodine titration methods was 4.02 ±0.02 (see Villalobos *et al.*, 2003, for details). Here, a value of 3.80 ±0.03 has been measured at pH 7 and low Ni content (NidBi2-7), suggesting the presence of Mn^{3+} or Mn^{2+}. The presence of Mn^{3+} both within the octahedral layer and as interlayer species at TC and TE sites is supported by chemical, bond valence, and XRD results which consistently show that Mn^{2+} occurs only as a minor interlayer species if present at all. In particular, the presence of Mn^{2+} at TC or TE sites is not consistent with the coordination of interlayer Mn cations determined from XRD modelling requiring the mean Mn-O bond length to be ~0.15 Å longer than in the proposed structure model (Table 2). Although δ-MnO_2 was equilibrated at pH 8 in the previous study, the 0.2 difference in Mn mean oxidation state is likely experimental because the oxalate and iodine methods used previously are less accurate than the Mohr salt / sodium pyrophosphate method used here (Gaillot, 2002). This hypothesis was verified by re-measuring the original δ-MnO_2 sample (pH 8) studied by Villalobos *et al.* (2006) with the second titration method. A new value of 3.88 ±0.03 was obtained, consistent with the 3.80 ±0.03 value measured for NidBi2-7 taking into account the decrease in mean oxidation degree of manganese with decreasing pH observed here and for soil manganese oxides (Negra *et al.*, 2005). Note also that the new model yielded a better fit to XRD data (R_{wp} = 6.2% – GoF ~ 4.6) than the previous model (R_{wp} = 10.7% – GoF ~ 9.4). The second difference, which derives directly from the lower mean oxidation degree of Mn, is the presence of Mn^{3+} in the interlayer. Multivalent cations in TC and TE sites are more efficient at compensating the charge deficit of most undersaturated O_{layer} atoms than Na^+ and H^+ only, as in the previous model. The presence of multivalent cations at TC positions is also consistent with other structural studies

355 on δ-MnO_2 and vernadite (Manceau *et al.*, 2007b; Peacock and Sherman, 2007b; Lanson *et*
356 *al.*, 2008). Third, the new model has 18% vacant layer sites, compared to 6% for the δ-MnO_2
357 sample studied previously. However, the new value does not reflect the actual number of
358 vacant sites in the layer when CSDs are small in the *a*-*b* plane (Webb *et al.*, 2005). Here, with
359 a CSD size of ~55 Å, compared to ~120 Å previously, a large fraction of Ni atoms is sorbed
360 on border sites as ^{DC}Ni complex when Ni/Mn > 1% (Fig. 2 – Manceau *et al.*, 2007b). This
361 complex increases the apparent number of layer vacancies seen by XRD because it has 2-3
362 nearest Mn neighbours instead of 6 for ^{TC}Ni on basal planes. Thus, the δ-MnO_2 crystals
363 studied here have fewer layer vacancies than determined by XRD, because some of them are
364 actually border sites. The distinction between interlayer and border sites becomes flimsy when
365 crystals are vanishingly small.
366
367 **Acknowledgments**
368
369 The authors are grateful to Alain Plançon for the unrestricted access to his XRD simulation
370 program. Camille Daubord and Delphine Tisserand are thanked for assistance with sample
371 preparation and chemical analyses, respectively. The three anonymous reviewers and AE
372 Karen Hudson-Edwards are thanked for their constructive remarks and suggestions. The
373 Université Joseph Fourier supported this study through its Pôle TUNES.
374

References

Angeli, F., Delaye, J.M., Charpentier, T., Petit, J.C., Ghaleb, D. and Faucon, P. (2000) Influence of glass chemical composition on the Na-O bond distance: a ^{23}Na 3Q-MAS NMR and molecular dynamics study. *Journal of Non-Crystalline Solids*, **276**, 132-144.

Aplin, A.C. and Cronan, D.S. (1985) Ferromanganese oxide deposits from the Central Pacific Ocean, I. Encrustations from the Line Islands Archipelago. *Geochimica et Cosmochimica Acta*, **49**, 427-436.

Attfield, J.P., Cheetham, A.K., Cox, D.E. and Sleight, A.W. (1988) Synchrotron X-ray and neutron powder diffraction studies of the structure of α-$CrPO_4$. *Journal of Applied Crystallography*, **21**, 452-457.

Bodeï, S., Manceau, A., Geoffroy, N., Baronnet, A. and Buatier, M. (2007) Formation of todorokite from vernadite in Ni-rich hemipelagic sediments. *Geochimica et Cosmochimica Acta*, **71**, 5698-5716.

Bogdanov, Y.A., Gurvich, E.G., Bogdanova, O.Y., Ivanov, G.V., Isaeva, A.B., Murav'ev, K.G., Gorshkov, A.I. and Dubinina, G.I. (1995) Ferromanganese nodules of the Kara Sea. *Oceanology*, **34**, 722-732.

Boonfueng, T., Axe, L. and Xu, Y. (2005) Properties and structure of manganese oxide-coated clay. *Journal of Colloid and Interface Science*, **281**, 80-92.

Brese, N.E. and O'Keeffe, M. (1991) Bond-valence parameters for solids. *Acta Crystallographica*, **B47**, 192-197.

Bricker, O. (1965) Some stability relations in the system Mn-O_2-H_2O at 25° and one atmosphere total pressure. *American Mineralogist*, **50**, 1296-1354.

399 Brown, I.D. (1977) Predicting bond lengths in inorganic crystals. *Acta Crystallographica*,
400 **B33**, 1305-1310.
401 Brown, I.D. (1996) VALENCE : a program for calculating bond valences. *Journal of Applied*
402 *Crystallography*, **29**, 479-480.
403 Chukhrov, F.V., Sakharov, B.A., Gorshkov, A.I., Drits, V.A. and Dikov, Y.P. (1985) Crystal
404 structure of birnessite from the Pacific ocean. *International Geology Review*, **27**,
405 1082-1088.
406 Delville, A. (1992) Structure of liquids at a solid interface: an application to the swelling of
407 clay by water. *Langmuir*, **8**, 1796-1805.
408 Drits, V.A. and Tchoubar, C. (1990) *X-ray diffraction by disordered lamellar structures :*
409 *theory and applications to microdivided silicates and carbons*. Springer-Verlag,
410 Berlin, 371 pp.
411 Drits, V.A., Silvester, E., Gorshkov, A.I. and Manceau, A. (1997) Structure of synthetic
412 monoclinic Na-rich birnessite and hexagonal birnessite. I. Results from X-ray
413 diffraction and selected-area electron diffraction. *American Mineralogist*, **82**, 946-961.
414 Drits, V.A., Lanson, B. and Gaillot, A.-C. (2007) Birnessite polytype systematics and
415 identification by powder X-ray diffraction. *American Mineralogist*, **92**, 771-788.
416 Exon, N.F., Raven, M.D. and De Carlo, E.H. (2002) Ferromanganese nodules and crusts from
417 the Christmas Island region, Indian Ocean. *Marine Georesources & Geotechnology*,
418 **20**, 275 - 297.
419 Feitknecht, W.M. and Marti, W. (1945) Über Manganite und künstlichen Braunstein.
420 *Helvetica Chimica Acta*, **28**, 149-156.
421 Gaillot, A.-C. (2002) *Caractérisation structurale de la birnessite: Influence du protocole de*
422 *synthèse*. Ph.D. thesis, Université Joseph Fourier - Grenoble I, Grenoble, France, 392
423 pp.

Gaillot, A.-C., Flot, D., Drits, V.A., Manceau, A., Burghammer, M. and Lanson, B. (2003) Structure of synthetic K-rich birnessite obtained by high-temperature decomposition of $KMnO_4$. I. Two-layer polytype from 800°C experiment. *Chemistry of Materials*, **15**, 4666-4678.

Gaillot, A.-C., Drits, V.A., Manceau, A. and Lanson, B. (2007) Structure of the synthetic K-rich phyllomanganate birnessite obtained by high-temperature decomposition of $KMnO_4$: Substructures of K-rich birnessite from 1000 °C experiment. *Microporous and Mesoporous Materials*, **98**, 267-282.

Gaillot, A.-C., Lanson, B. and Drits, V.A. (2005) Structure of birnessite obtained from decomposition of permanganate under soft hydrothermal conditions. 1. Chemical and structural evolution as a function of temperature. *Chemistry of Materials*, **17**, 2959-2975.

Giovanoli, R. (1969) A simplified scheme for polymorphism in the manganese dioxides. *Chimia*, **23**, 470-472.

Giovanoli, R. (1980) Vernadite is random-stacked birnessite. *Mineralia Deposita*, **15**, 251-253.

Howard, S.A. and Preston, K.D. (1989) Profile fitting of powder diffraction patterns. Pp. 217-275 in *Modern Powder Diffraction* (D.L. Bish and J.E. Post, editors). *Reviews in Mineralogy and Geochemistry*, **20**. Mineralogical Society of America, Chantilly, Va.

Huang, X., Yue, H., Attia, A. and Yang, Y. (2007) Preparation and Properties of Manganese Oxide/Carbon Composites by Reduction of Potassium Permanganate with Acetylene Black. *Journal of The Electrochemical Society*, **154**, A26-A33.

Jurgensen, A., Widmeyer, J.R., Gordon, R.A., Bendell-Young, L.I., Moore, M.M. and Crozier, E.D. (2004) The structure of the manganese oxide on the sheath of the

448 bacterium *Leptothrix discophora*: An XAFS study. *American Mineralogist*, **89**, 1110-
449 1118.
450 Koschinsky, A. and Halbach, P. (1995) Sequential leaching of marine ferromanganese
451 precipitates: Genetic implications. *Geochimica et Cosmochimica Acta*, **59**, 5113-5132.
452 Koschinsky, A. and Hein, J.R. (2003) Uptake of elements from seawater by ferromanganese
453 crusts: solid-phase associations and seawater speciation. *Marine Geology*, **198**, 331-
454 351.
455 Lanson, B., Drits, V.A., Silvester, E. and Manceau, A. (2000) Structure of H-exchange
456 hexagonal birnessite and its mechanism of formation from Na-rich monoclinic
457 buserite at low pH. *American Mineralogist*, **85**, 826-838.
458 Lanson, B., Drits, V.A., Feng, Q. and Manceau, A. (2002a) Structure of synthetic Na-
459 birnessite: Evidence for a triclinic one-layer unit cell. *American Mineralogist*, **87**,
460 1662-1671.
461 Lanson, B., Drits, V.A., Gaillot, A.-C., Silvester, E., Plancon, A. and Manceau, A. (2002b)
462 Structure of heavy-metal sorbed birnessite: Part 1. Results from X-ray diffraction.
463 *American Mineralogist*, **87**, 1631-1645.
464 Lanson, B., Marcus, M.A., Fakra, S., Panfili, F., Geoffroy, N. and Manceau, A. (2008)
465 Formation of Zn-Ca phyllomanganate nanoparticles in grass roots. *Geochimica et*
466 *Cosmochimica Acta*, **72**, 2478-2490.
467 Lei, G. and Boström, K. (1995) Mineralogical control on transition metal distributions in
468 marine manganese nodules. *Marine Geology*, **123**, 253-261.
469 Lingane, J.J. and Karplus, R. (1946) New method for determination of manganese. *Industrial*
470 *and Engineering Chemistry. Analytical Edition*, **18**, 191-194.

471 Manceau, A., Drits, V.A., Silvester, E., Bartoli, C. and Lanson, B. (1997) Structural
472 mechanism of Co^{2+} oxidation by the phyllomanganate buserite. *American*
473 *Mineralogist*, **82**, 1150-1175.
474 Manceau, A., Lanson, B. and Drits, V.A. (2002) Structure of heavy metal sorbed birnessite.
475 Part III: Results from powder and polarized extended X-ray absorption fine structure
476 spectroscopy. *Geochimica et Cosmochimica Acta*, **66**, 2639-2663.
477 Manceau, A., Tommaseo, C., Rihs, S., Geoffroy, N., Chateigner, D., Schlegel, M., Tisserand,
478 D., Marcus, M.A., Tamura, N. and Chen, Z.-S. (2005) Natural speciation of Mn, Ni,
479 and Zn at the micrometer scale in a clayey paddy soil using X-ray fluorescence,
480 absorption, and diffraction. *Geochimica et Cosmochimica Acta*, **69**, 4007-4034.
481 Manceau, A., Kersten, M., Marcus, M.A., Geoffroy, N. and Granina, L. (2007a) Ba and Ni
482 speciation in a nodule of binary Mn oxide phase composition from Lake Baikal.
483 *Geochimica et Cosmochimica Acta*, **71**, 1967-1981.
484 Manceau, A., Lanson, M. and Geoffroy, N. (2007b) Natural speciation of Ni, Zn, Ba, and As
485 in ferromanganese coatings on quartz using X-ray fluorescence, absorption, and
486 diffraction. *Geochimica et Cosmochimica Acta*, **71**, 95-128.
487 Mandernack, K.W., Post J. and Tebo, B.M. (1995) Manganese mineral formation by bacterial
488 spores of the marine *Bacillus* strain SG-1: Evidence for the direct oxidation of Mn(II)
489 to Mn(IV) . *Geochimica et Cosmochimica Acta*, **59**, 4393-4408.
490 McMurdie, H.F. (1944) Microscopic and diffraction studies on dry cells and their raw
491 materials. *Transactions of the Electrochemical Society*, **86**, 313-326.
492 McMurdie, H.F. and Golovato E. (1948) Study of the Modifications of Manganese Dioxide.
493 *Journal of Research of the National Institute of Standards and Technology*, **41**, 589-
494 600.

495 Miyata, N., Maruo, K., Tani, Y., Tsuno, H., Seyama, H., Soma, M. and Iwahori, K. (2006)
496 Production of biogenic manganese oxides by anamorphic Ascomycete fungi isolated
497 from streambed pebbles. *Geomicrobiology Journal*, **23**, 63-73.
498 Negra, C., Ross, D.S. and Lanzirotti, A. (2005) Oxidizing Behavior of Soil Manganese:
499 Interactions among Abundance, Oxidation State, and pH. *Soil Science Society of*
500 *America Journal*, **69**, 87-95.
501 Peacock, C.L. and Sherman, D.M. (2007a) Crystal-chemistry of Ni in marine ferromanganese
502 crusts and nodules. *American Mineralogist*, **92**, 1087-1092.
503 Peacock, C.L. and Sherman, D.M. (2007b) Sorption of Ni by birnessite: Equilibrium controls
504 on Ni in seawater. *Chemical Geology*, **238**, 94-106.
505 Plançon, A. (2002) CALCIPOW: a program for calculating the diffraction by disordered
506 lamellar structures. *Journal of Applied Crystallography*, **35**, 377.
507 Post, J.E. and Veblen, D.R. (1990) Crystal structure determinations of synthetic sodium,
508 magnesium, and potassium birnessite using TEM and the Rietveld method. *American*
509 *Mineralogist*, **75**, 477-489.
510 Silvester, E., Manceau, A. and Drits, V.A. (1997) Structure of synthetic monoclinic Na-rich
511 birnessite and hexagonal birnessite. II. Results from chemical studies and EXAFS
512 spectroscopy. *American Mineralogist*, **82**, 962-978.
513 Tebo, B.M., Bargar, J.R., Clement, B.G., Dick, G.J., Murray, K.J., Parker, D., Verity, R. and
514 Webb, S.M. (2004) Biogenic Manganese Oxides: Properties and Mechanisms of
515 Formation. *Annual Review of Earth and Planetary Sciences*, **32**, 287-328.
516 Tebo, B.M., Johnson, H.A., McCarthy, J.K. and Templeton, A.S. (2005) Geomicrobiology of
517 manganese(II) oxidation. T*rends in Microbiology*, **13**, 421-428.

518 Tournassat, C., Charlet, L., Bosbach, D. and Manceau, A. (2002) Arsenic(III) oxidation by
519 birnessite and precipitation of manganese(II) arsenate. *Environmental Science and*
520 *Technology*, **36**, 493-500.
521 Vetter, K.J. and Jaeger, N. (1966) Potentialausbildung an der Mangandioxid-Elektrode als
522 oxidelektrode mit nichtstochiometrischem oxid. *Electrochimica Acta*, **11**, 401-419.
523 Villalobos, M., Toner, B., Bargar, J. and Sposito, G. (2003) Characterization of the
524 manganese oxide produced by *Pseudomonas putida* strain MnB1. *Geochimica et*
525 *Cosmochimica Acta*, **67**, 2649-2662.
526 Villalobos, M., Bargar, J. and Sposito, G. (2005) Mechanisms of Pb(II) Sorption on a
527 Biogenic Manganese Oxide. *Environmental Science & Technology*, **39**, 569-576.
528 Villalobos, M., Lanson, B., Manceau, A., Toner, B. and Sposito, G. (2006) Structural model
529 for the biogenic Mn oxide produced by *Pseudomonas putida*. *American Mineralogist*,
530 **91**, 489-502.
531 Webb, S.M., Tebo, B.M. and Bargar, J.R. (2005) Structural characterization of biogenic Mn
532 oxides produced in seawater by the marine *Bacillus sp*. strain SG-1. *American*
533 *Mineralogist*, **90**, 1342-1357.
534 Webster, R. (2001) Statistics to support soil research and their presentation. *European*
535 *Journal of Soil Science*, **52**, 331-340.
536 Xu, J.J. and Yang, J. (2003) Nanostructured amorphous manganese oxide cryogel as a high-
537 rate lithium intercalation host. *Electrochemistry Communications*, **5**, 230-235.
538

Figure captions

FIG. 1. XRD patterns of Ni-sorbed δ-MnO_2. (**a**) pH 4. (**b**) pH 7. The grey bar indicates a 5× scale factor for the high-angle region except for samples NidBi56-7 and NidBi177-7 (1.67× scale factor). For each pH series, the sample with the lowest Ni/Mn ratio is systematically shown as a light grey line to emphasize the modification of XRD traces with Ni content (arrows).

FIG. 2. Schematic representation of layer and interlayer sites reported in the literature for metal cations (including Mn) in δ-MnO_2. TC, DC and TE labels refer respectively to triple-corner sharing, double-corner sharing and triple-edge sharing sites. E label refers to layer sites.

FIG. 3. Simulations of the 11,20, 31,02 and 22,40 X-ray scattering bands (C-centred layer cell) for Ni-sorbed δ-MnO_2 samples. Black crosses are experimental data, solid grey overplots are calculated profiles, and solid lines at the bottom are difference plots. Structural parameters used for the simulations are listed in Tables 2, and 3.

FIG. 4. Structure model of Ni-sorbed δ-MnO_2. (**a**) Projection on the *a*-*b* plane. (**b**) Projection on the *b*-*c** plane. Shaded octahedra represent layer Mn and its coordination sphere. Bonds between interlayer species and coordinating oxygens are shown in ball-and-stick. The coordinates of the different species along the *c** axis are given in Å.

FIG. 5. Simulations of the 31,02 X-ray scattering band (C-centred layer cell) for sample NidBi105-4. Gray crosses are experimental data, and lines are calculated profiles. The

564 optimum fit to the data (solid line) was obtained with b = 2.835 Å and $a = \sqrt{3} \times b$ (Table 2).
565 Varying b by ± 0.01 Å with $a = \sqrt{3} \times b$ significantly decreases the fit quality. The inset shows
566 the evolution of R_{wp} with b.
567
568 FIG. 6. Simulations of the 001 and 002 diffraction lines for Ni-sorbed δ-MnO_2. Patterns
569 as in Figure 4. Structural parameters used for the simulations are listed in Tables 2 and 3.
570
571 FIG. 7. Average oxidation degree of Mn as a function of Ni/Mn ratio for Ni-sorbed δ-
572 MnO_2 samples (circles: pH 4, triangles: pH 7).

TABLE 1. Chemical composition of Ni-sorbed δ-MnO_2 expressed as atomic ratios.

Sample	Na/Mn (%)	Ni/Mn (%)	Mn Ox.	Layer Mn^{3+}
NidBi2-4	18.39 ±0.30	0.23 ±0.23	3.74 ±0.03	0.09
NidBi11-4	16.99 ±0.27	1.07 ±0.23	3.73 ±0.03	N.D.
NidBi50-4	10.90 ±0.05	4.97 ±0.04	3.75 ±0.02	0.08
NidBi105-4	5.57 ±0.15	10.57 ±0.15	3.77 ±0.02	0.07
NidBi2-7	26.53 ±0.19	0.25 ±0.14	3.80 ±0.03	0.04
NidBi11-7	26.80 ±0.40	1.07 ±0.24	3.80 ±0.03	N.D.
NidBi56-7	20.87 ±0.22	5.66 ±0.15	3.85 ±0.02	0.01
NidBi177-7	7.61 ±0.22	17.78 ±0.21	3.94 ±0.01	0.00

Note: Mn Ox. stands for "oxidation degree". Layer Mn^{3+} is calculated from the average oxidation degree of Mn and from the number of interlayer Mn atoms (Table 3), which are considered to be trivalent. Uncertainties on the mean values are calculated as the mean of standard errors (Webster, 2001). Sample names as in Manceau *et al.* (2007b)

TABLE 2. Crystal data for Ni-sorbed δ-MnO_2.

	NidBi2-4	NidBi50-4	NidBi105-4	NidBi2-7	NidBi56-7	NidBi177-7
a (Å)	4.916	4.912	4.910	4.917	4.919	4.917
b (Å)	2.838	2.836	2.835	2.839	2.840	2.839
d(001) (Å)	7.3	7.3	7.3	7.3	7.3	7.3
Average CSD along c^* (Å)	11.0	10.2	9.5	12.4	15.3	11.0
CSD in the *a*-*b* plane (Å)[a]	56	54	54	54	54	50
R_{wp} (%)[b]	5.72-6.32	4.12-5.17	4.97-5.00	8.74-6.15	5.22-5.82	5.21-6.06
GoF (%)[b]	6.49-4.53	3.57-3.32	5.41-3.33	15.40-4.45	8.42-6.52	5.41-4.17

[a] Diameter of the disk-like coherent scattering domains. [b] First and second values are calculated over the low- and high-angle regions, respectively.

TABLE 3. Structural parameters of Ni-sorbed δ-MnO_2 derived from XRD.

Atom	x[a]	y	z	ζ[b]	Occ.[c] NidBi2-4	Occ.[c] NidBi50-4	Occ.[c] NidBi105-4	Occ.[c] NidBi2-7	Occ.[c] NidBi56-7	Occ.[c] NidBi177-7
Mn_{layer} (Mn1)	0.000	0.000	0.000	0.000	0.82	0.82	0.82	0.82	0.815	0.84
O_{Mn1} (O1)	0.333	0.000	0.139	1.015	2.00	2.00	2.00	2.00	2.00	2.00
^{TC}Mn (Mn2)	0.000	0.000	0.299	2.183	0.14	0.16	0.16	0.10	0.085	0.07
H_2O_{Mn2} (O2)	-0.333	0.000	0.472	3.446	0.42	0.48	0.48	0.30	0.255	0.21
^{TE}Mn (Mn3)	-0.333	0.000	0.299	2.183	0.03	0.00	0.00	0.05	0.04	0.00
H_2O_{Mn3} (O3)	0.000	0.000	0.472	3.446	0.09	0.00	0.00	0.15	0.12	0.00
^{TC}Ni (Ni1)	0.000	0.000	0.306	2.234	0.00	0.04	0.07	0.00	0.05	0.13
H_2O_{Ni1} (O4)	-0.333	0.000	0.486	3.548	0.00	0.12	0.21	0.00	0.15	0.39
^{TE}Ni (Ni2)	-0.333	0.000	0.315	2.300	0.00	0.02	0.02	0.00	0.00	0.02
H_2O_{Ni2} (O5)	0.000	0.000	0.486	3.548	0.00	0.06	0.06	0.00	0.00	0.06
$Na_{interlayer}$ (Na)[d]	-0.525	0.000	0.500	3.650	0.18	0.06	0.06	0.24	0.18	0.06
H_2O_{Na+} (O6)[e]	0.200	0.000	0.500	3.650	0.54	0.18	0.18	0.72	0.54	0.18

[a] Atomic coordinates x, y, z are expressed as fractions of the a, b and d(001) parameters, respectively. Positions are given in the (x, 0, z) form. Equivalent positions are (x + ½, ½, z), because the unit cell is C-centred. Additional equivalent positions are (-x, 0, -z). [b] Coordinates along the c* axis, ζ, are expressed in Å to emphasize the thickness of layer and interlayer polyhedra. [c] Occupancies are given per half

formula unit as the sum of the occupancies for all equivalent positions. [d] Additional symmetry operations: (-*x*/2 - ½, 3*x*/2 + ½, *z*), and (-*x*/2 - ½, -3*x*/2 - ½, *z*). [e] Additional symmetry operations: (-*x*/2, 3*x*/2, *z*), and (-*x*/2, -3*x*/2, *z*).

Unrefined Debye-Waller thermal factors (B) are equal to 0.5 for Mn_{layer}, 1.0 for O_{layer}, interlayer Mn and Ni, 1.5 for H_2O molecules bound to interlayer Mn and Ni, and 2.0 for other interlayer species (alkali cations and H_2O molecules).

TABLE 4. Bond valences calculated[a] for Ni-sorbed δ-MnO_2

	O1[b]	O1[c]	O1[d]	O1[e]	O2/O3	O4/O5	O6	Σ	Formal valence
Mn1	0.625 ×6→ ×3↓	0.625 ×2↓	0.625 ×2↓	0.625 ×2↓				3.75	4
Mn2, Mn3		0.509 ×3→			0.433 ×3→			2.8	3
Ni1, Ni2			0.298-0.352[f] ×3→			0.300-0.317[f] ×3→		1.9	2
Na^+				0.091 0.012 ×2→			0.261, 0.053, 0.045[g]	0.5	1
H^+				0.105[h]	0.815 ×2↓	0.815 ×2↓	0.815 ×2↓		
Σ	1.9	1.8	1.5-1.6[f]	1.3-1.4[i]	2.1	1.9	1.7-1.9[g]		

[a] Bond valences in valence unit (v.u.) were calculated using the Valence for Dos program (v. 2.0 - http://www.ccp14.ac.uk/solution/bond_valence/index.html – Brown, 1996) and the parameters from Brese and O' Keeffe (1991). [b] O1 coordinated to 3 Mn^{4+} in Mn1 (Table 3). [c] O1 coordinated to 2 Mn^{4+} in Mn1 and 1 Mn^{3+} in Mn2 or Mn3 (Table 3). [d] O1 coordinated to 2 Mn^{4+} in Mn1 and 1 Ni^{2+} in Ni1 or Ni2 (Table 3). [e] O1 coordinated to 2 Mn^{4+} in Mn1 (Table 3). [f] Depending on whether Ni is located in Ni1 or in Ni2. [g] Na^{+} is coordinated to 3 H_2O molecules at 2.30, 2.89, and 2.95 Å. [h] O6-H-O1 H-bond. [i] Depending on whether this O1 receives additional valence from Na^{+} or from H^{+} through H-bond.

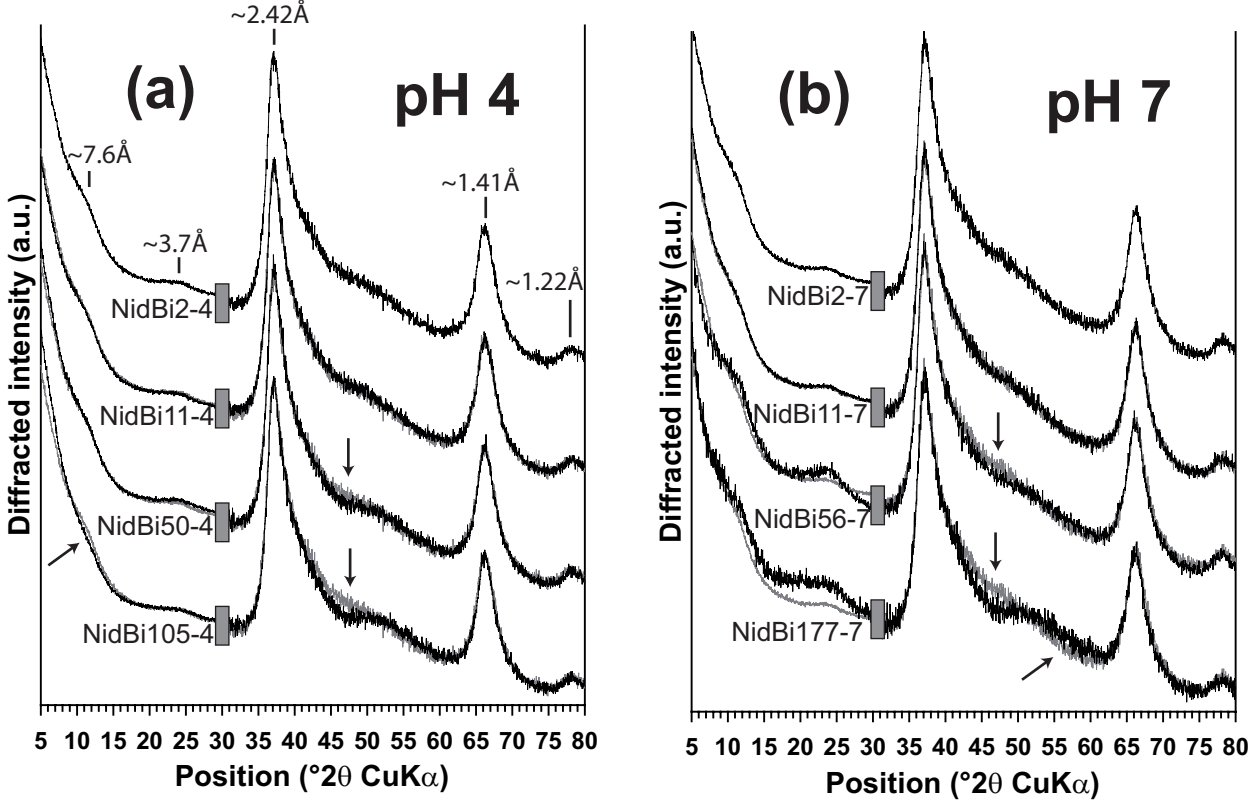
(a)
pH 4
~2.42Å
~7.6Å
~3.7Å
~1.41Å
~1.22Å
NidBi2-4
NidBi11-4
NidBi50-4
NidBi105-4
Diffracted intensity (a.u.)
5 10 15 20 25 30 35 40 45 50 55 60 65 70 75 80
Position (°2θ CuKα)
(b)
pH 7
NidBi2-7
NidBi11-7
NidBi56-7
NidBi177-7
Diffracted intensity (a.u.)
5 10 15 20 25 30 35 40 45 50 55 60 65 70 75 80
Position (°2θ CuKα)

Figure 1

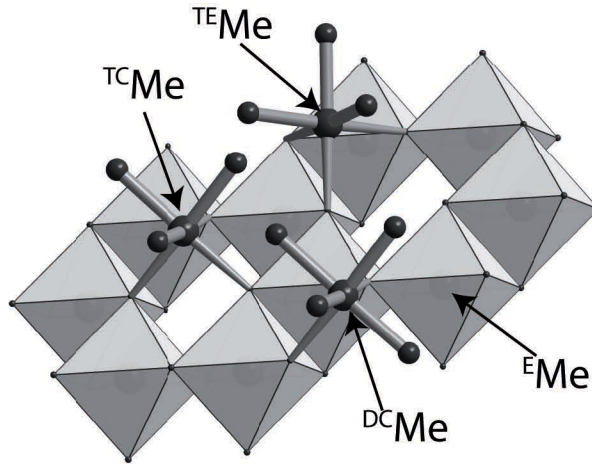

Figure 2

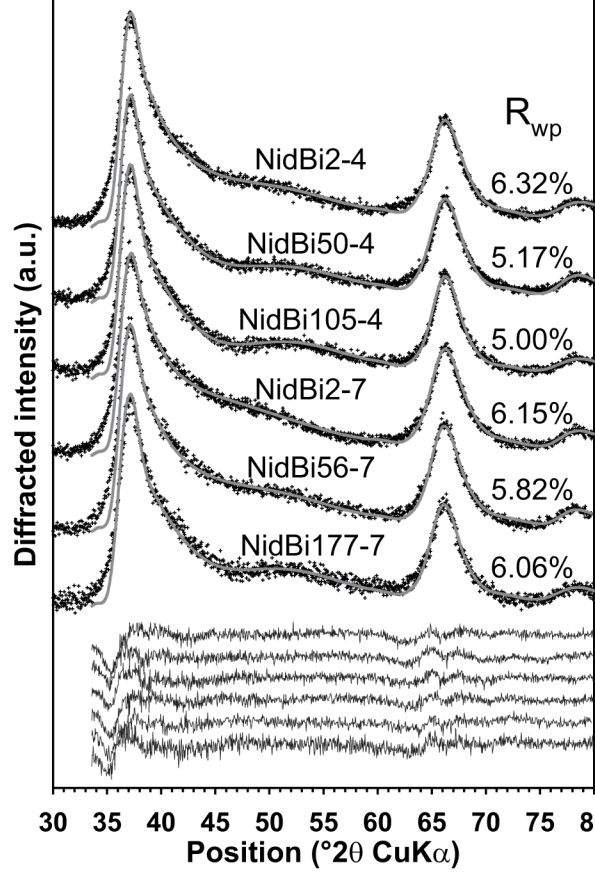
Diffracted intensity (a.u.)
R_wp
NidBi2-4
6.32%
NidBi50-4
5.17%
NidBi105-4
5.00%
NidBi2-7
6.15%
NidBi56-7
5.82%
NidBi177-7
6.06%
30 35 40 45 50 55 60 65 70 75 80
Position (°2θ CuKα)

Figure 3

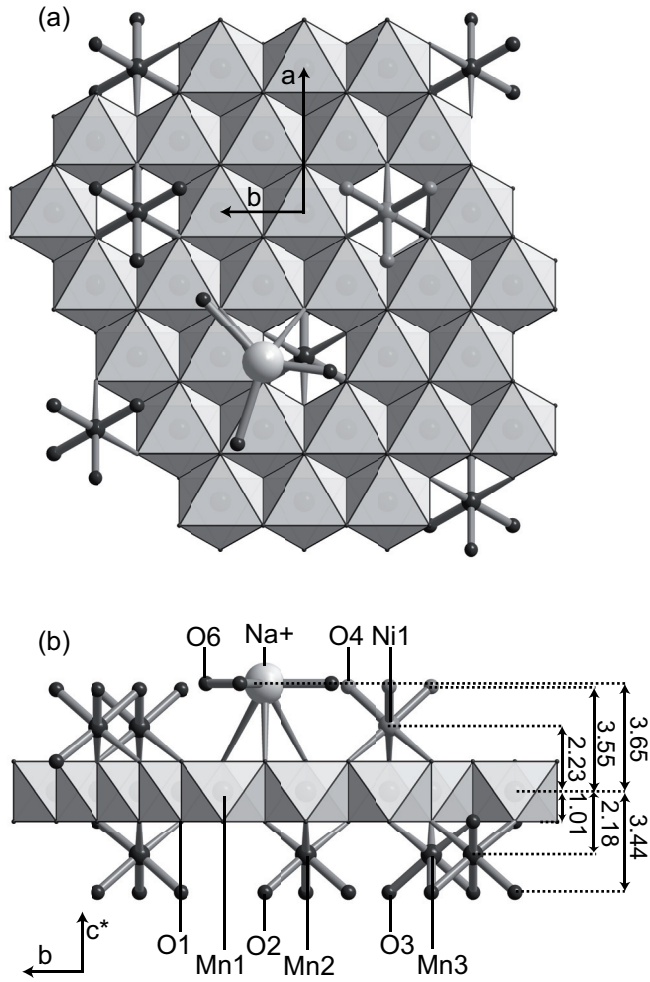

Figure 4

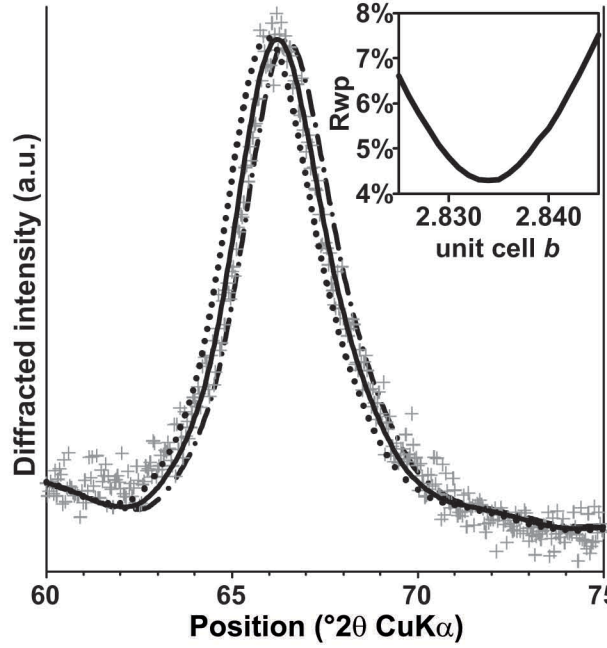
Diffracted intensity (a.u.)
60
65
70
75
Position (°2θ CuKα)
8%
7%
6%
5%
4%
Rwp
2.830
2.840
unit cell b

Figure 5

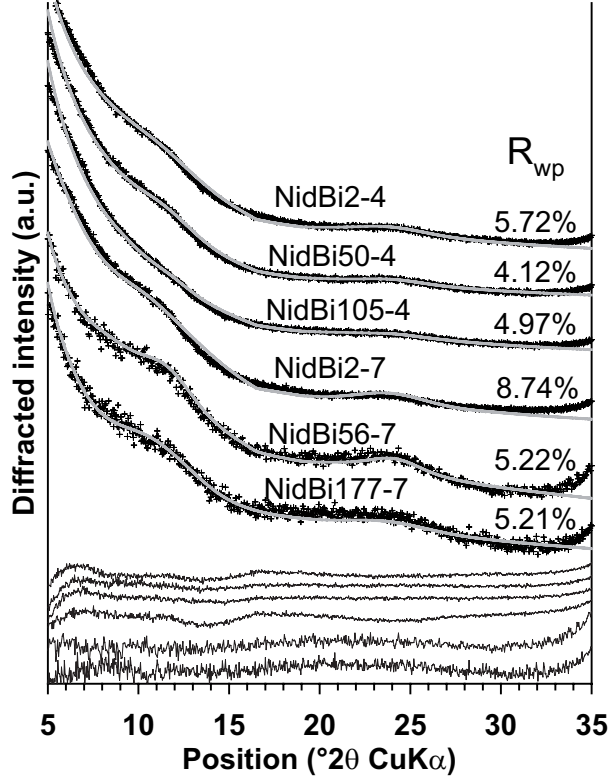
Diffracted intensity (a.u.)
R_wp
NidBi2-4
5.72%
NidBi50-4
4.12%
NidBi105-4
4.97%
NidBi2-7
8.74%
NidBi56-7
5.22%
NidBi177-7
5.21%
5
10
15
20
25
30
35
Position (°2θ CuKα)

Figure 6

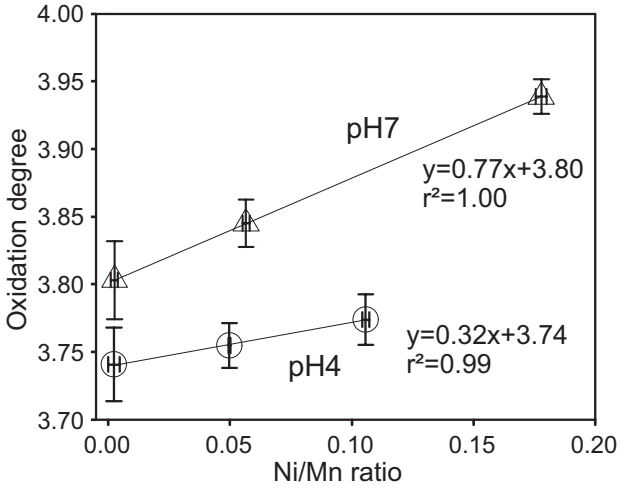
4.00
3.95
3.90
3.85
3.80
3.75
3.70
Oxidation degree
0.00
0.05
0.10
0.15
0.20
Ni/Mn ratio
pH7
y=0.77x+3.80
r²=1.00
pH4
y=0.32x+3.74
r²=0.99

Figure 7